Received: 12 November 2020 | Revised: 23 February 2021 | Accepted: 26 March 2021 | Published on: 19 April 2021

DOI: 10.1002/qj.4032

Quarterly Journal of the Royal Meteorological Society RMetS

RESEARCH ARTICLE

A cold pool perturbation scheme to improve convective initiation in convection-permitting models

Mirjam Hirt | **George C. Craig**

Meteorological Institute, Ludwig-Maximilians Universität, München, Germany

Correspondence
Mirjam Hirt, Meteorological Institute, Ludwig-Maximilians Universität, München 80333, Germany.
Email: m.hirt@lmu.de

Abstract

Cold pools originate from evaporation in precipitating downdraughts and spread as density currents at the surface. Vertical motion at the leading edge of the cold pool is an important trigger for new convective cells in organised convective storms. However, these motions are poorly resolved at the grid lengths of a kilometre or more used in convection-permitting models. Consequently, the simulated gust fronts do not trigger enough new convection, leading to precipitation deficits and a lack of convective organization. To address these deficits, we introduce a cold pool perturbation (CPP) scheme that strengthens vertical velocity at the simulated cold pool gust fronts. This is achieved by relaxing the vertical velocity in the gust front region towards a target value derived from similarity theory. Applying the CPP scheme for simulations of a highly convective 10-day period, we find increased precipitation amplitudes during the afternoon. There is also evidence for improvements in the location of precipitation and for stronger organization of convection, although substantial errors remain. The cold pools themselves become more frequent, larger and more intense. An additional potentially beneficial influence was found for convective initiation at sea breeze fronts.

KEYWORDS

cold pools, convective organization, deep convection, density currents, gust fronts

1 | INTRODUCTION

The simulation and prediction of convective precipitation relies heavily on convection-permitting models. These models have horizontal grid sizes of a few kilometres or less, which allows them to simulate the circulations associated with deep convective clouds explicitly, rather than using a cumulus parametrization scheme. Although the convective clouds are not well-resolved at these grid lengths, the improvement over simplistic representations in the parametrizations has led to a step change in the quality of simulations and predictions of deep convection and the associated precipitation (Baldauf *et al.*, 2011; Clark *et al.*, 2016). Despite their high computational requirements, convection-permitting models are now affordable for a wide range of applications. They are already well

established for regional operational weather prediction (Baldauf *et al.*, 2011; Clark *et al.*, 2016), and are being tested for regional climate simulations (Leutwyler *et al.*, 2017; Schär *et al.*, 2019), and recently even as global models (Judt, 2018; Stevens *et al.*, 2019; Zhou *et al.*, 2019; Dueben *et al.*, 2020). It is expected that convection-permitting models will become even more important in the future (ECMWF, 2016; Palmer, 2019).

Despite the clear benefits of using kilometre-scale resolution, the simulated convective precipitation is still far from perfect. A delayed onset of convective precipitation during the day has been identified (Baldauf *et al.*, 2011; Clark *et al.*, 2016), as well as deficits in the structure of cloud objects (Hanley *et al.*, 2015; Senf *et al.*, 2018; Panosetti *et al.*, 2019; Stein *et al.*, 2020), and too little precipitation in the afternoon and evening (Rasp *et al.*, 2018; Hirt *et al.*, 2019), which is likely associated with a lack of persistent convective organization (Rasp *et al.*, 2018; Moseley *et al.*, 2020). These systematic errors could result from a number of different processes involved in deep convection, but which are either insufficiently resolved or rely on subgrid-scale parametrizations in these models. These processes include microphysical processes, entrainment, shallow–deep transition, and processes in the planetary boundary layer (PBL) which are essential for initiating convection.

One process that has received considerable attention is the initiation of convection. Convective initiation requires low-level air to reach its level of free convection. To do so, the air parcel typically has to overcome the Convective Inhibition (CIN), which requires triggering processes in the boundary layer or the local removal of CIN. This is usually achieved by PBL processes such as turbulence, orographic lifting, sea breezes or cold pools. However, these lifting processes tend to be too weak in models with resolutions of a kilometre or more. It has been found that adding perturbations of temperature and moisture to the boundary layer can substantially change convective initiation (Done *et al.*, 2006; Leoncini *et al.*, 2010; Flack *et al.*, 2018). This work provided the motivation for the physically based stochastic perturbation schemes PSP (Kober and Craig, 2016) and PSP2 (Hirt *et al.*, 2019), which use information from the boundary-layer turbulence scheme to add realistic levels of variability near the model resolution. The addition of these perturbations was found to improve the onset time and amount of precipitation during the day, but had less impact on the deficits in the organization of convection and on the afternoon/evening precipitation amounts.

Long-lived, organized convective systems do not rely on random turbulent perturbations to initiate convection, but are characterized by secondary initiation, generally associated with cold pools formed by existing convective cells. Cold pools are volumes of cold, dense air which result from evaporation in deep convective downdraughts. When these cold, dense downdraughts hit the surface, they spread as a density current in roughly circular patterns. The leading edge of these spreading cold pools often forms a gust front where ascending air can initiate new convection. This can occur due to mechanically driven lifting, as proposed by Rotunno *et al.* (1988); Weisman and Rotunno (2004), which is even stronger when two or more cold pools collide (Feng *et al.*, 2015; Cafaro and Rooney, 2018; Haerter *et al.*, 2018; Torri and Kuang, 2019; Meyer and Haerter, 2020), or due to moisture accumulation at cold pool boundaries, which increases buoyancy and reduces CIN (Tompkins, 2001). Cold pools can thus trigger new convection in the vicinity of existing storms, leading to the organization of convective cells, and provide a significant triggering mechanism late in the diurnal cycle.

Although models with resolution of a few kilometres can simulate cold pools explicitly, comparison with higher-resolution simulations shows that many aspects of cold pools are not well-represented and depend strongly on the grid spacing (Hirt *et al.*, 2020). In this study, it was found that, at lower resolutions, the size and intensity of cold pools reduces, while their frequency increases, consistent with results of Squitieri and Gallus (2020). Hirt *et al.* (2020) further found a reduced likelihood of cold pool gust fronts to trigger new convection at lower resolutions, which is mainly caused by gust front vertical velocities which are too weak. A causal graph analysis indicated that the weaker gust fronts are not attributable to the weaker cold pool intensities, as one might assume (Hirt *et al.*, 2020). Instead, weaker gust front vertical velocities are directly correlated to the model resolution, independent of other cold pool properties. Any feature with a size close to the model resolution will be smoothed across several grid points, which is a distance of several kilometres in a convection-permitting model. The broader, weaker gust front circulations that result at coarser resolution are less likely to bring low-level air to its level of free convection, and fewer convective cells are initiated. In addition to weaker gust fronts at low resolution, changes to the number and size of cold pools will affect the area occupied by gust fronts and the frequency of convective initiation. It seems plausible that improving the representation of cold pool processes has the potential to improve the simulated organization of convection and afternoon/evening precipitation amounts.

The aim of this paper is to develop a method for improving the representation of cold pool processes in convection-permitting models. In models with parametrized convection, the convective circulations are included in the parametrization, and it is natural to parametrize the cold pools as well (Rozbicki *et al.*, 1999;

Grandpeix and Lafore, 2010; Grandpeix *et al.*, 2010; Park, 2014). At higher resolution, the representation of cold pools becomes a grey-zone problem, where the circulations are partially resolved. Rather than parametrizing the cold pools as complete entities, we will attempt to modify the gust front circulations that already exist in these models to give more realistic convective initiation. Based on our earlier results (Hirt *et al.*, 2020; see summary in the previous paragraph) that the weak gust front circulations are not attributable to weak cold pool intensities, we will enhance the vertical velocity in gust front regions, which should lead directly to increased convective initiation. Although we do not explicitly alter other cold pool properties, an increase in cold-pool-driven convective initiation may further strengthen the original convective system and thereby enhance the cold pool size and intensity. This may in turn increase convective initiation, resulting in a feedback loop (Böing *et al.*, 2012; Schlemmer and Hohenegger, 2014).

The primary goals of this study are:

1. To develop a cold pool perturbation (CPP) scheme, which strengthens cold pool gust fronts and improves cold-pool-driven convective initiation.
2. To describe and quantify the impact of CPP on the simulated convection, including most importantly the convective organization and the afternoon/evening precipitation amounts.

The CPP scheme will be developed in the context of the convection-permitting COSMO model, which until recently was the operational high-resolution model of the German weather service (DWD). Two main challenges must be addressed. The first is to determine how strong the vertical motion in the gust fronts should be, to give the amplitude of the perturbations. The second is to identify the horizontal and vertical regions where the gust front ascent occurs, to define the location of the perturbations. The impact of the CPP scheme will be evaluated by comparing 24 hr simulations with radar observations over Germany for a ten-day convective weather period in spring 2016. In addition to the evolution of the precipitation rates over the diurnal cycle, diagnostics related to the location and structure of the cold pools and precipitation will be considered.

This paper is structured as follows. First, we give a short overview of the selected days and the simulation strategy in Section 2. We formulate the CPP scheme in Section 3, based on a simple theoretical analysis of the resolution dependence of cold pool gust fronts in Section 3.1. We evaluate the impact of the CPP scheme and its performance during a 10-day period in Section 4, followed by a short description of its parameter sensitivity in Section 5. We end with a discussion in Section 6.

2 | MODEL SIMULATIONS, SIMULATION PERIOD AND DIAGNOSTICS

2.1 | Model and simulation set-up

Simulations are computed with the COSMO (COnsortium for Small-scale MOdeling) model (Baldauf *et al.*, 2011), version 5.4g, in a convection-permitting set-up with a horizontal grid size of $\Delta x = 0.025°$, roughly 2.8 km, and a time step of 25 s, with 461 by 421 grid points centred over Germany at 10°E, 50°N. The 50 vertical model layers are stretched from 10 m above ground to 22 km above mean sea level. The staggered grid (Arakawa-C/Lorenz) uses a terrain-following vertical coordinate (Schättler *et al.*, 2016). While deep convection is not parametrized, the Tiedtke parametrization scheme is used for shallow convection. Further details on parametrizations can be found in Doms *et al.* (2011). This set-up is identical to the one used in Hirt *et al.* (2019) and, except for a change in the tuning parameter `tur_len` (Hirt *et al.*, 2019 give details), closely follows the operational set-up.

As initial conditions, we take the deterministic analysis from the COSMO-KENDA ensemble data assimilation system (Schraff *et al.*, 2016), which uses a local ensemble transform Kalman filter for conventional observations and latent heat nudging for radar observations. Using the high-resolution analysis reduces model spin-up in comparison to using downscaled initial conditions. We use global ICON forecasts for boundary conditions and start 24-hr simulations at 0000 UTC on each of the simulation days.

A simulation without the CPP scheme is denoted as *Reference*.

2.2 | Simulation period

To present the CPP scheme and its qualitative impact, we focus on a single day, 5 June 2016 over Germany. This day is chosen based on the frequent occurrence of cold pools and associated characteristic errors in precipitation. To systematically evaluate the impact of the CPP scheme in different weather situations, we consider the 10-day period from 29 May to 7 June 2016, which was characterized by heavy precipitation over Germany in different synoptic situations (Piper *et al.*, 2016). The first five days were dominated by an upper-level trough and associated low-pressure systems over Germany. During this period, synoptically driven lifting and southeasterly advection of moist air caused heavy rainfall, particularly on 30 May. The last five days of the 10-day period were dominated by a persistent omega-blocking event with the ridge centred over

Europe. Weak synoptic forcing allowed substantial convective instability to build up each day, followed by strong convection.

Due to the intense convective activity and high variability in the synoptic forcing, this period has been considered in a number of studies of convection (Baur *et al.*, 2018; Rasp *et al.*, 2018; Bachmann *et al.*, 2019; Hirt *et al.*, 2019; Keil *et al.*, 2019) and provides a good testing ground for the CPP scheme. As in Hirt *et al.* (2019), we separate the ten days into five days with stronger synoptic forcing and five days with weaker synoptic forcing to evaluate the adaptation of the scheme to different synoptic conditions.

2.3 | Observations and diagnostics

To evaluate potential improvements of the CPP scheme in the model, we compare our simulations to precipitation fields derived from radar observations. We use quality-controlled radar observations, namely the Radar Online Aneichung (RADOLAN) EY product provided by the German Weather Service. This radar product uses European radar reflectivities and provides radar coverage for most of our domain (Deutscher Wetterdienst, 2018a; 2018b).

For comparisons between simulations and radar observations, we restrict the geographical region to grid points with available radar data. To evaluate the simulated precipitation, we compute hourly aggregated, domain-averaged precipitation, the Fraction Skill Score (FSS; Roberts and Lean 2008, the Structure component of the SAL score (S-SAL; Wernli *et al.*, 2008; 2009) and cell sizes where we identify precipitation objects as regions with precipitation larger than a certain threshold ($5\,\mathrm{mm{\cdot}hr^{-1}}$). Details on the computational setup and the computation of the S-SAL score can be found in Appendix B and C, respectively. We further detect cold pool objects using a detection algorithm based on density potential temperature anomalies and precipitation, closely following the algorithm from Hirt *et al.* (2020). Further details can be found in Appendix D.

3 | COLD POOL PERTURBATIONS

The goal of the CPP scheme is to enable lower-resolution simulations to emulate the cold pool gust fronts of high-resolution simulations. Specifically, the vertical velocity at cold pool gust fronts should produce similar vertical velocities to those of of fully resolved gust fronts. To achieve this, we first estimate a characteristic vertical velocity scale for fully resolved gust fronts, w_0, in Section 3.1, using dimensional analysis. This target vertical velocity scale w_0 is then used in the subsequent subsections to build appropriate cold pool perturbations for the numerical model.

3.1 | Scale of gust front vertical velocity

The classical analysis of a spreading density current predicts a propagation speed of $U = \sqrt{2BH}$, where B is a characteristic scale for the buoyancy perturbation of the cold pool and H is the depth scale (e.g., von Kármán, 1940; Benjamin, 1968; Bryan and Rotunno, 2008; Markowski and Richardson, 2011, chapter 5.3.2). If the influences of rotation and stratification are small in the PBL, we anticipate that the flow at the leading edge of the gust front will be isotropic, so that the vertical velocity will follow the same scaling. In a recent paper, Reif *et al.* (2020) derived a more general scaling that includes the effects of boundary-layer stratification and the slope of the leading edge of the gust front. They found that w will be modified by a factor $K \sin\alpha$, where K is an internal Froude number (a measure of stratification) and α is the angle between the gust front boundary and the ground. Typical values of K range between 0.7 and 1.4, while α was found to lie in the range from 30 to 45°. In the present work, we ignore variations in boundary-layer stratification and gust front slope, and absorb the resulting constant factor into the overall scaling parameter α_{cp} defined in Section 3.3. We note however that the analysis of Reif *et al.* (2020) shows how the slope and stratification effects could be incorporated if their variations are found to be important to convective initiation.

We focus on how coarse horizontal resolution leads to weaker gust front vertical velocities. In such a model, features will be smoothed in the horizontal over a distance of several times the horizontal grid length. If the grid length is a kilometre or more, the horizontal length-scale of the circulation will be much larger than the vertical scale, which is related to the cold pool depth of a few hundred metres at most, and the vertical velocity will be correspondingly weaker. A dimensional analysis based on the two-dimensional Boussinesq equations can be used to estimate the strength of the vertical motion driven by a horizontal buoyancy contrast when the horizontal length-scale L is different from the vertical scale H. As shown in Appendix A, the resulting vertical velocity scale W is given by

$$W = \sqrt{\frac{BH}{1 + \frac{L^2}{H^2}}}. \tag{1}$$

In the case of a fully resolved gust front, we expect $L/H \approx 1$. This expectation is supported by idealized cold

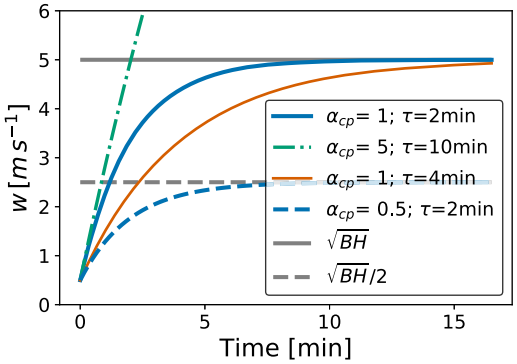

FIGURE 1 Schematic illustration of the temporal evolution of w and how it depends on τ_{cp} and α_{cp}. Here, we consider the idealized situation of $\partial w/\partial t|_{cp}$ without any other effects when w_0 remains constant. The target vertical velocity $\alpha_{cp}\sqrt{BH}$ is set to $5\alpha_{cp}$ ($\mathrm{m{\cdot}s^{-1}}$) and the initial model vertical velocity to $0.5\,\mathrm{m{\cdot}s^{-1}}$ [Colour figure can be viewed at wileyonlinelibrary.com]

pool simulations, for example in Grant and van den Heever (2016) and following Jeevanjee (2017). Then we obtain a characteristic vertical velocity scale w_0:

$$w_0 = \sqrt{\frac{BH}{2}}. \tag{2}$$

This is consistent with the classical estimate, differing only by a constant of order 1.

3.2 | The basic approach of CPP

The main objective of the CPP scheme is to increase the vertical velocities at cold pool gust fronts to a value consistent with the target vertical velocity scale w_0. One way to do this would be to multiply the model vertical veolicty w by a factor $\sqrt{1+L^2/H^2}$, as suggested by Equation (1), however this could lead to instabilities with w increasing without bound. Instead, we apply tendency perturbations $\partial w/\partial t|_{cp}$ to w at gust fronts so that its amplitude will converge to the target w_0 on a time-scale determined by τ_{cp}:

$$\left.\frac{\partial w}{\partial t}\right|_{cp} = \frac{1}{\tau_{cp}}(w_0 - w). \tag{3}$$

The relaxation of w to the target value is schematically illustrated in Figure 1 for the idealized situation where all other processes affecting w are neglected and w_0 remains constant. The figure illustrates how the vertical velocity evolution will depend on the relaxation time-scale τ_{cp}, as well as other parameters.

Given this general design of CPP, several details must be considered. These are addressed separately in the following subsections:

Section 3.3 Estimating w_0 from model fields.
Section 3.4 Considering the vertical distribution of the perturbations, as w_0 only provides a height-independent characteristic scale.
Section 3.5 Finding a reasonable time-scale τ_{cp}.
Section 3.6 Confining perturbations to cold pool gust fronts.

We summarize the complete CPP scheme in Section 3.7

3.3 | Estimating w_0 from model fields

To compute the target vertical velocity for CPP, $w_0 = \sqrt{BH/2}$, we have to approximate the cold pool buoyancy B and its height H. Examination of model cross-sections show that the height of the buoyancy anomaly of cold pools within the COSMO simulations is typically about 200 m (not shown). For simplicity, we fix H to this value. As we cannot easily identify cold pools online in the model, we approximate the cold pool buoyancy using the local horizontal buoyancy gradient in the lowest model level multiplied by the width of the gradient. In particular, we assume that gradients extend over the scale of the effective model resolution of $5\Delta x$. Thus B is given by:

$$B = |\nabla_h \theta_v| 5\Delta x \; g \; \frac{1}{\theta_v}. \tag{4}$$

Doing so, we obtain $\sqrt{BH}$ with values of up to $\mathcal{O}(10\,\mathrm{m{\cdot}s^{-1}})$ at cold pool gust fronts, as displayed in Figure 2b. This is significantly stronger than that currently simulated for w with the model (Figure 2a), and can be regarded as the upper limit since processes such as friction or entrainment were neglected in the derivation of w_0. In general, a dimensional analysis aims to show the dependence of a solution on the key scales defining the problem, while the magnitudes will deviate from the exact solution by an order-one factor which depends on the precise configuration of the system. To account for these details, we introduce a tuning parameter α_{cp}, so that

$$w_0 = \alpha_{cp}\sqrt{BH}. \tag{5}$$

If the construction of CPP is physically consistent, α_{cp} should be of magnitude $\mathcal{O}(1)$ and should not require retuning for other weather situations and model set-ups. Figure 1 shows in an idealized framework how different values of α_{cp} impact the evolution of w by changing the target vertical velocity.

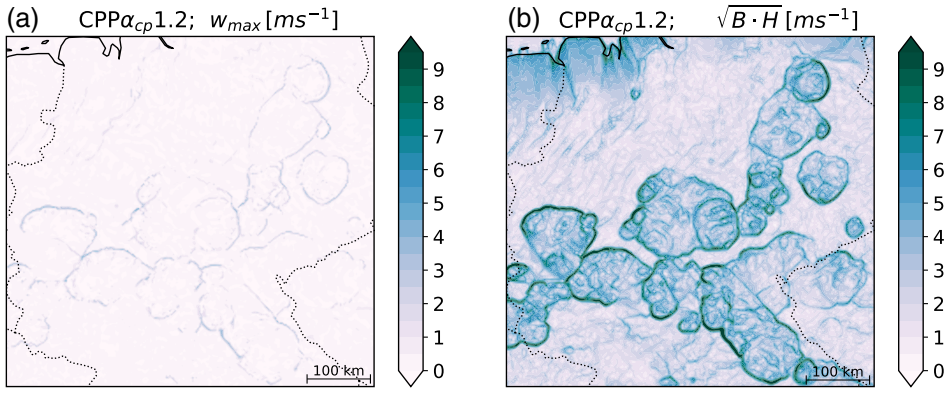

FIGURE 2 Comparison of (a) maximum vertical velocity $w_{\max}$ in the lowest kilometre at the surface and (b) the target vertical velocity $w_0 = \sqrt{BH}$ ($\alpha_{cp} = 1$) as approximated from θ_v gradients. Fields are shown for 5 June 2016 at 1500 UTC [Colour figure can be viewed at wileyonlinelibrary.com]

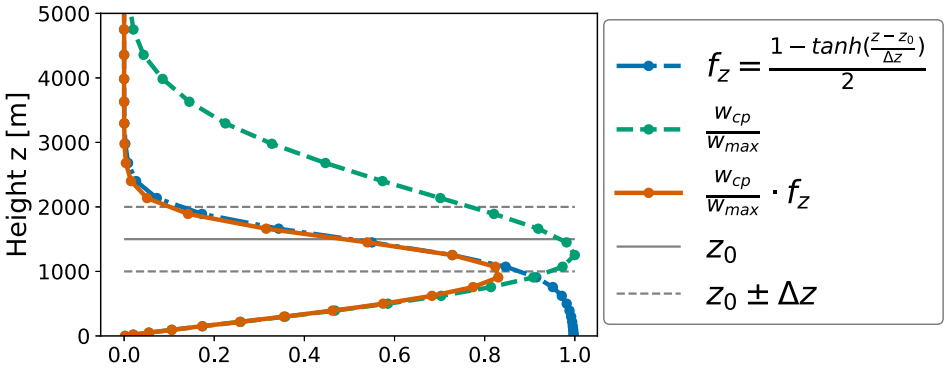

FIGURE 3 Vertical behaviour of the CPP scheme for a conceptual, but representative, w_{cp}/w_{max} profile. See text for details [Colour figure can be viewed at wileyonlinelibrary.com]

3.4 | Vertical distribution of the perturbations

As the characteristic scale w_0 does not include any information on the vertical distribution, we will use the vertical distribution from the model vertical velocity itself to scale $\partial w/\partial t|_{cp}$. To do so, we compare w_0 to the maximum vertical velocity w_{max} from the surface to a fixed model level $k^* = 38$, corresponding to a height of approximately 1,070 m. This limit is imposed to avoid comparing w_0 to the large vertical velocities found in cumulus updraughts above the boundary layer. We assume that the difference between w_0 and w_{max} applies to the other model levels in a multiplicative way:

$$\left.\frac{\partial w}{\partial t}\right|_{cp} = \frac{\left(\alpha_{cp}\sqrt{BH} - w_{max}\right)}{\tau_{cp}} \frac{w(z)}{w_{max}}. \quad (6)$$

Hence, the perturbations depend in the vertical on $w(z)/w_{max}$, as illustrated by the green dashed line in Figure 3.

We also restrict the perturbations to the lower atmosphere, where the gust fronts are active. To do so, we multiply the perturbations by a function

$$f(z) = 0.5\left[1 - \tanh\left(\frac{z - z_0}{\Delta z}\right)\right]$$

which gradually reduces the perturbations to zero at a height z_0 within a height range of $\mathcal{O}(\Delta z)$. In Figure 3, $f(z)$ is illustrated by the blue dash-dotted line and the resulting perturbation profile by the orange solid line. We have tested several different possibilities for z_0 and Δz and use z_0=1,500 m and Δz=500 m. As the example shows, the combination of this function with the vertical profile of w in the model w_{cp}/w_{max} may lead to a target w-profile with a slightly reduced maximum value (maximum of the orange solid curve in Figure 3).

3.5 | Time-scale τ_{cp}

The time-scale τ_{cp} describes the characteristic time-scale on which the target vertical velocity is approached under isolated situations. In practice, however, the response of the model to our vertical velocity perturbations is likely reduced due to pressure perturbations (Fiedler, 2002; Chagnon and Bannon, 2005; Edson and Bannon, 2008) and numerical diffusion, resulting in a reduced effectiveness of the perturbations. This will likely increase the effective time-scale. Furthermore, the target vertical velocity is not constant in time but follows the movement of the gust front. If the characteristic speed of movement is 10 m·s^{-1}, and the model fields vary over a distance of 5Δx, the time-scale for changes due to gust front

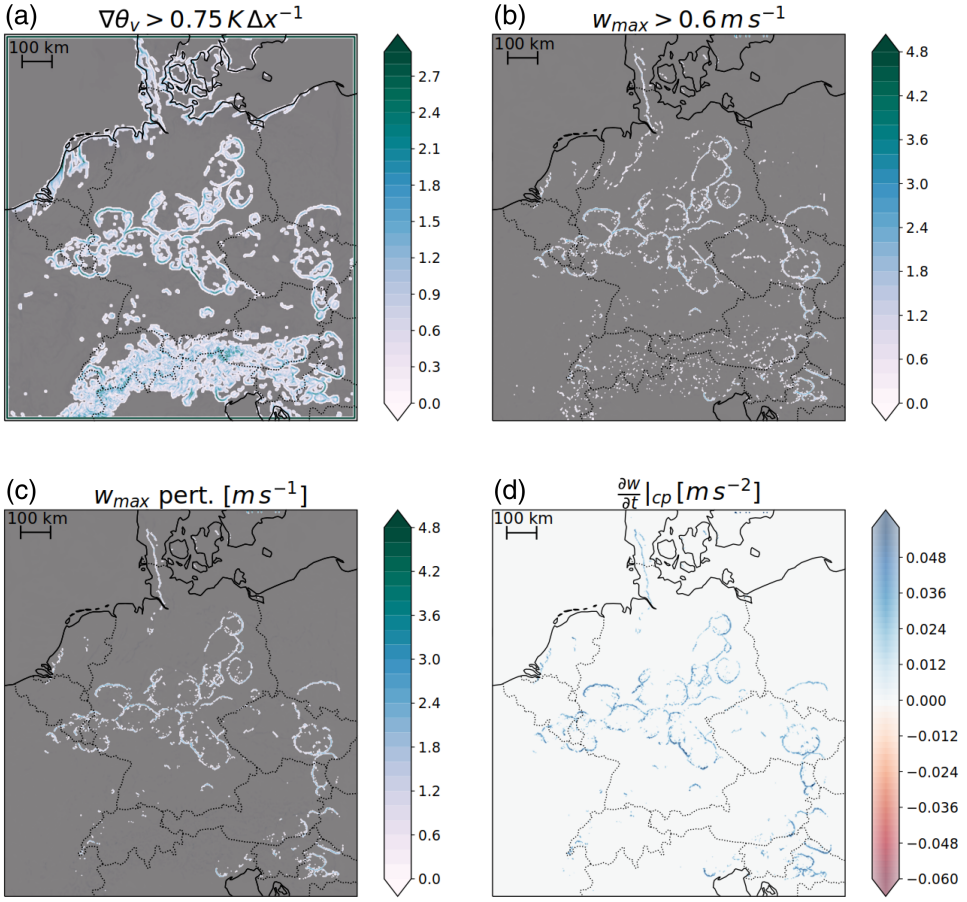

FIGURE 4 Illustration of how the perturbations are constrained to cold pool gust fronts. In (a), the buoyancy gradients are displayed with the applied mask (i.e., 0.75 K·Δx^{-1} threshold and horizontal filter) in grey shading. In (b), w_{max} is shown with values smaller 0.6 m·s^{-1} shaded grey. In (c), $w_{\max}$ is shaded using the first two criteria combined with the orography criterion. In (d), the final perturbations for $\partial w/\partial t$ are shown [Colour figure can be viewed at wileyonlinelibrary.com]

movement can be approximated as $\tau_{\text{advective}} = 5\Delta x/10$ m · s^{-1} ≈23 min. For gust fronts to be effectively strengthened throughout their lifetime, the time-scale τ_{cp} should be as short as possible, and must be shorter than the advective time-scale of $\mathcal{O}$(10 min). On the other hand, the time-scale must be long enough to be resolved by the model time step of 25 s. We will consider values of τ_{cp} in $\mathcal{O}$(1 min).

As illustrated in Figure 1, the short-term impact of changing τ_{cp} in an idealized framework can also be compensated by changing α_{cp} (e.g., the green dash-dotted line and blue bold line are similar for the first minute).

3.6 | Selecting cold pool gust fronts using a mask $\mathcal{M}_{\text{gf}}$

Finally, the vertical velocity perturbations have to be constrained to cold pool gust fronts. An object-based identification of cold pools or cold pool gust front as in Hirt *et al.* (2020) is computationally expensive, so we instead identify grid points that belong to cold pool gust fronts using a set of four local criteria.

First, we select grid points with strong virtual potential temperature gradients, that is, grid points with $|\nabla_{\text{h}}\theta_{\text{v}}|$ larger than $\theta^*_{\text{v,g}}$ =0.75 K·Δx^{-1}. As this intermediate criterion can be quite noisy, we apply a uniform, horizontal filtering with $n_{\text{filter}} = 3$ grid boxes filter size to the criterion itself. A $|\nabla_{\text{h}}\theta_{\text{v}}|$ field with the corresponding, horizontally smoothed, conditional mask is shown in Figure 4a for illustration. Second, we select grid points with strong vertical velocities, that is, with $w_{\max}$ larger than $w^*_{\max}$ = 0.5 m·s^{-1}, as illustrated in Figure 4b (no filtering is applied here).

These two criteria already show the characteristic bow-structures of the cold pool gust fronts. However, many active grid points over orographic regions are visible, which are not associated with cold pools. As a third condition, we exclude these orographic regions by requiring the standard deviation of subgrid-scale orographic height μ_{sso} at each grid point to be below a threshold $\mu^*_{\text{sso}} = 50$ m, thereby using μ_{sso} as a proxy for resolved orographic variability.

Finally, we only select grid columns, where the model vertical velocity $w_{\max}$ is lower than the target vertical velocity w_0. The resulting horizontal mask with the first three criteria applied simultaneously is displayed in Figure 4c. Most active grid points seem to be related to cold pool gust fronts, as indicated by the bow-like structures. Aside from a few spurious active grid points, it is interesting to note that the sea breeze is partially included, which will be

investigated and discussed in more detail in Sections 4.4 and 6. We will refer to this gust front mask as $\mathcal{M}_{\text{gf}}$, with values of 1 for active perturbations and 0 otherwise.

3.7 | Summary of the full CPP set-up

We can now summarize the CPP scheme as

$$\left.\frac{\partial w}{\partial t}(x,y,z,t)\right|_{\text{cp}} = \frac{(\alpha_{\text{cp}}\sqrt{BH} - w_{\max})}{\tau_{\text{cp}}}\frac{w(z)}{w_{\max}}f(z)\mathcal{M}_{\text{gf}}, \quad (7)$$

where the different variables can be described as:

$$B(x,y,t)\text{: approx. cold pool buoyancy,} \quad (8)$$

$$w_{\max}(x,y,t|k^*)\text{: max. } w \text{ in the lowest, levels up to } k^*, \quad (9)$$

$$w(x,y,z,t)\text{: model vertical velocity,} \quad (10)$$

$$f(z|H_0,\Delta H)\text{: function to vertically limit CPP to the lower troposphere,} \quad (11)$$

$$\mathcal{M}_{\text{gf}}(x,y,t|w^*_{\max},\theta^*_{\text{v,g}},n_{\text{filter}},\mu^*_{\text{sso}})\text{: binary mask to limit CPP to gust fronts.} \quad (12)$$

The parameters and their default values are listed in Table 1. An example of the vertical velocity perturbations using the default parameter values is displayed in Figure 4d. In addition to the default values, we also consider simulations with $\alpha_{\text{cp}} = 2$ and test the sensitivity to other parameters (τ_{cp}, $w_{\max}$ and H_0) in Section 5.

4 | IMPACT OF THE CPP SCHEME

We now evaluate the impact of the CPP scheme. To do so, we consider some example fields mainly on 5 June 2016 and several quantitative diagnostics applied to the whole 10-day period. While we focus mostly on cold pool gust fronts and precipitation fields (amplitude, location and organization), we will show that CPP also impacts cold pools and the sea breeze.

4.1 | Cold pool gust fronts

The most direct effect of CPP is expected on the cold pool gust fronts. Figure 5 shows vertical velocity at ≈1 km above the surface for an example time step. In comparison to the reference run, the gust fronts, that is, the line structures of positive vertical velocity (blue), are enhanced, with higher vertical velocities in the CPP simulation. We also find more pronounced downward branches of the gust fronts (red line structures). These amplifications indicate that the whole gust front circulation is strengthened, although the CPP perturbations only affect the upward branch. We have confirmed that the displayed behaviour is also visible at other times and days when cold pools occur. As Figure 2 shows, however, the target vertical velocity is not fully reached at the cold pool gust fronts in the simulations. Such behaviour could be due to the dynamic evolution of cold pool gust fronts, or due to pressure perturbations that render the perturbations less effective (Fiedler, 2002; Chagnon and Bannon, 2005; Edson and Bannon, 2008). Nonetheless, the gust front vertical velocities decrease/increase with lower/higher amplitudes α_{cp} (not shown, see Jupyter notebooks), confirming the role of α_{cp} as a tuning parameter. We conclude that the first intention of the

TABLE 1 Parameters of CPP and their default values

Parameter	Default value	Description
$\boldsymbol{\alpha_{\text{cp}}}$	1.2	Scaling parameter
$\boldsymbol{\tau_{\text{cp}}}$	120 s	Adjustment time-scale
k^*	38 ≈ 1 km	Maximum height level for searching $w_{\max}$
H	200 m	Cold pool height used for determining target w_0
$\mathbf{H_0}$	1,500 m	Height at which to set perturbations to zero
ΔH	500 m	Height range for gradually setting perturbations to zero
$\mathbf{w^*_{max}}$	0.6 m·s^{-1}	Threshold for $w_{\max}$ to select gust fronts
$\theta^*_{\text{v,g}}$	0.75 K·Δx^{-1}	Threshold for θ_{v} gradient to select gust fronts
n_{filter}	3 Δx	Filter size for smoothing θ_{v} gradient selection
μ^*_{sso}	50 m	Threshold for selecting only non-orographic grid points

Note: Parameters in bold font are considered for parameter sensitivity tests (Section 5).

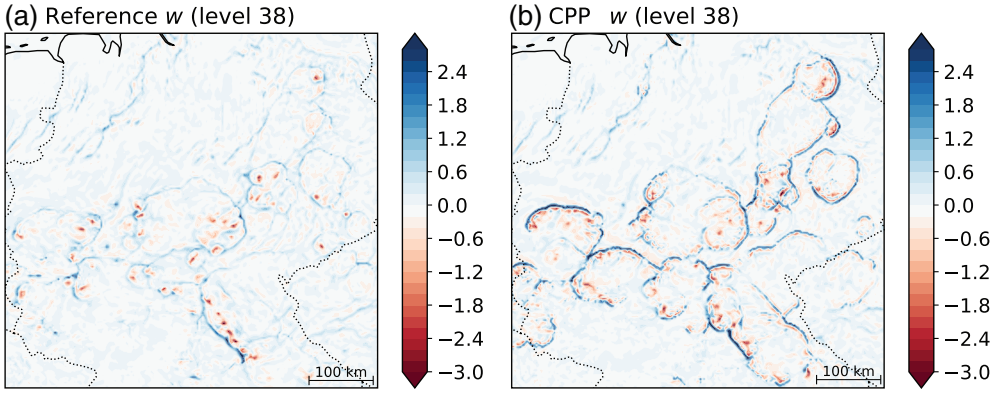

FIGURE 5 Vertical velocity for (a) the reference and (b) the default CPP simulation. Fields are displayed for the 38th model level (≈1 km) at 1500 UTC and a selected region with several cold pool gust fronts over central Germany

CPP – namely to strengthen cold pool gust fronts – is generally achieved.

4.2 | Impact on precipitation

Given the stronger cold pool gust fronts with the CPP scheme, we expect more new deep convection to be initiated by cold pools, which subsequently should also affect the precipitation fields. To corroborate this expectation, we now investigate the impact of CPP on precipitation in more detail. Considering example precipitation fields, we see the biggest differences in the late afternoon and evening, when cold pools are more frequent. Fields for 5 June 2016 at 1700 UTC are displayed in Figure 6 for illustration. Overall, the large-scale structures of the precipitation fields are similar for both the reference and the default CPP simulation ($\alpha_{cp} = 1.2$) but differences in the details can be found. There is more precipitation with CPP than in the reference simulations; the precipitation cells seem to be stronger and larger, and they form more pronounced line structures or are more clustered together. The black boxes show two examples of this enhanced organization in the CPP simulation. These effects are even more apparent with larger perturbation amplitudes $\alpha_{cp} = 2$ (Figure 6d). To confirm these differences, the performance of the simulated precipitation is evaluated more quantitatively in the following paragraphs.

4.2.1 | Precipitation amplitude

The diurnal cycle of precipitation for CPP using the default parameter values is displayed in Figure 7a (blue line), and shows enhanced precipitation especially from 1200 to 1900 UTC for both the strongly and weakly forced period, confirming the previous visual impression of increased precipitation. A small reduction in precipitation is visible after 2000 UTC. The amplitude bias compared to the radar observations is reduced over most of the day for the weakly forced period, but strengthened for the strongly forced period.

4.2.2 | Spatial distribution of precipitation

To evaluate the spatial positioning of the simulated precipitation in comparison to observations, we consider the Fraction Skill Score (Roberts and Lean, 2008). The FSS compares the fractions of precipitating gridpoints (precipitation larger than a threshold of e.g., 0.1 mm·hr^{-1}) within a specified neighbourhood (scale) between model and radar data. Higher FSS values indicate more skill with FSS=1 indicating a perfect match. Values below ≈0.5 are assumed to be without useful skill. As Figure 7b shows for weakly forced days, CPP improves the FSS from 1200 to 1900 UTC by up to ≈0.07. This positive impact of CPP is relatively independent of the specific thresholds and scales used to compute the FSS (not shown) and suggests an improved positioning of the precipitation in comparison with the observations. For the strongly forced days, the impact is very small.

4.2.3 | Structure and organization of precipitation

To identify changes in the structure of precipitation cells, we compute the S-SAL score. The S(tructure) component of the SAL score is an object-based measure for the structure of the precipitation field (Wernli *et al.*, 2008; 2009). Negative S values imply that the simulated precipitation cells are too small and peaked compared to the radar observations while $S = 0$ suggests a perfect match in terms of structure. Details on the computation are given in Appendix C. Since we already consider the domain-aggregated precipitation amplitude and

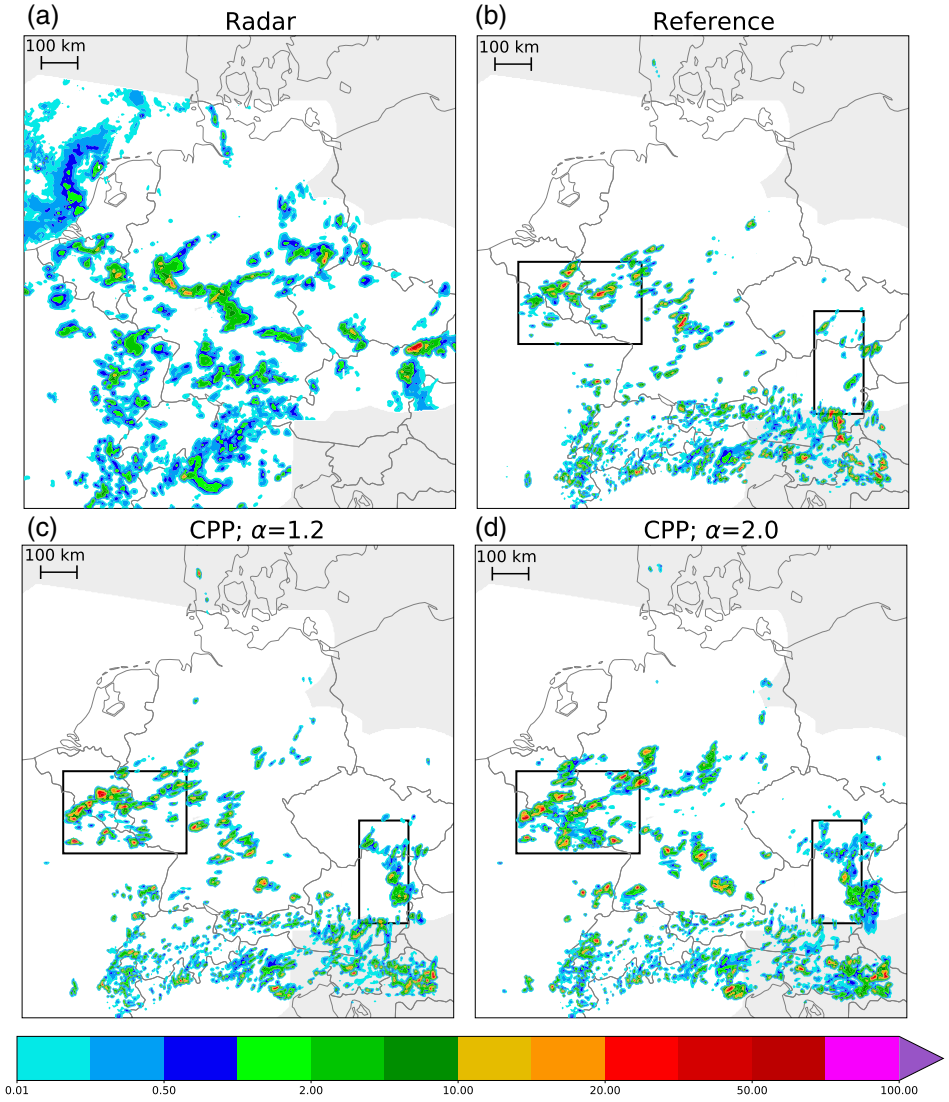

FIGURE 6 Example precipitation fields (mm·hr^{-1}) are shown for (a) radar observations, (b) the reference, (c) the default CPP simulation, and (d) a CPP simulation with $\alpha = 2$ on 5 June 2016 at 1700 UTC [Colour figure can be viewed at wileyonlinelibrary.com]

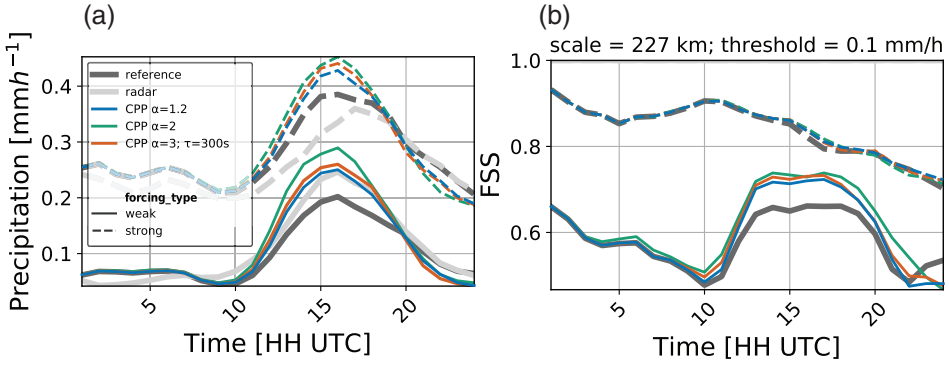

FIGURE 7 Diurnal cycle of (a) domain-averaged precipitation and (b) FSS averaged over the five weakly and five strongly forced days. For the FSS, a precipitation threshold of 0.1 mm·hr^{-1} and a scale of 227 km have been used. We have tested different settings as well, but the qualitative impact of CPP is not sensitive for most settings

FSS, we did not find additional value in analysing also the A(mplitude) and L(ocation) components of the SAL score. Figure 8a shows a small improvement in cell structures in the afternoon and evening for the weakly forced period, suggesting that precipitation cells are wider and less peaked. Again, this effect becomes even stronger for larger amplitudes α_{cp}. For the strongly forced period, the S-SAL score deteriorates slightly during the afternoon.

In Figure 8b, the average radii of precipitation cells (precipitation >5 mm·hr^{-1}) are displayed as another proxy for area-based convective organization. For both forcing periods, the cell radii are slightly larger than in the

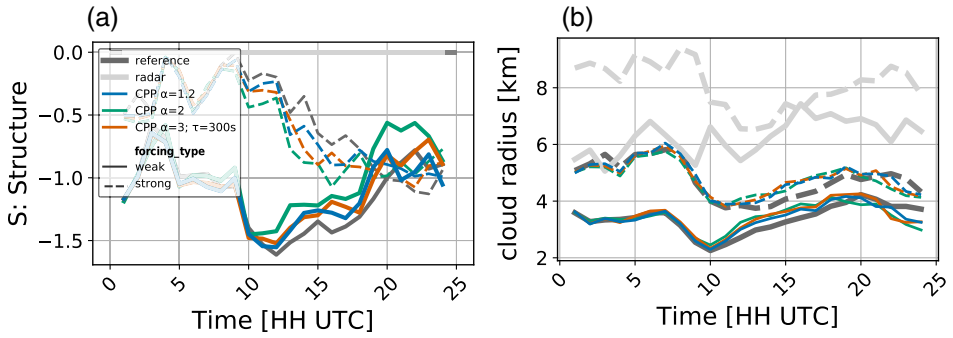

FIGURE 8 (a) S component of the SAL score and (b) average precipitation cell radius, with cells identified as precipitating areas with a precipitation threshold of 5 mm·hr^{-1} [Colour figure can be viewed at wileyonlinelibrary.com]

reference simulation. Both the S-SAL score and the cell radii still show large discrepancies between the CPP simulation and the radar observations. Nonetheless, the CPP scheme mostly improves these metrics, thereby indicating slightly more organized precipitation and confirms our visual impression from Figure 6.

The quantitative impact of CPP on precipitation generally corroborates our expectations that CPP effectively strengthens cold pool gust fronts, thereby enhancing cold-pool-driven convective initiation and strengthening precipitation cells, precipitation amplitude and convective organization. This appears to be beneficial especially for the weakly forced period, when local trigger mechanisms are more important.

4.3 | Impact on cold pools

Enhanced convective initiation at cold pool gust fronts may also be able to strengthen the cold pools themselves by intensifying and extending the lifetime of the original precipitation cells. To evaluate this possibility, we consider the frequency and characteristics of cold pool objects in the different simulations. As shown in Figure 9a, cold pools are more frequently detected in the afternoon and in the weak forcing period in all simulations. We expect that stronger surface heating in the afternoon and during the weak forcing period enables stronger temperature gradients at the surface and hence more cold pools. This frequency distribution is also consistent with the stronger impact of CPP on precipitation in the afternoon and the weak forcing period. Figure 9 also shows that cold pool numbers increase with CPP, that cold pools are more intense as measured by their negative density potential temperature anomaly, and that they are larger than in the reference simulation. For a higher perturbation amplitude $\alpha_{cp} = 2$, even stronger effects are found. These findings emphasize the relevance of the positive feedback effect of cold-pool-driven convective initiation leading to more intense cold pools, further enhancing convective initiation.

4.4 | Impact on the sea breeze

Perhaps unexpectedly, Figure 4 shows active CPP perturbations on the sea breeze near the coast. Although CPP is designed for cold pools, sea breezes are in some respects similar to density currents and can initiate convection. Examination of fields of precipitation and vertical velocity

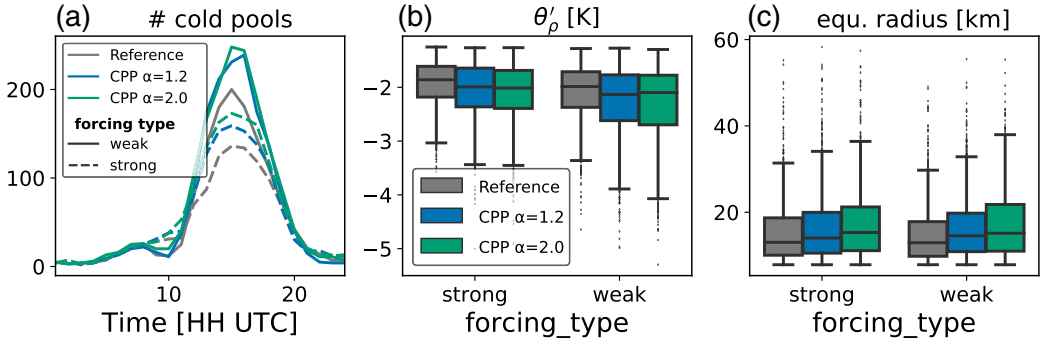

FIGURE 9 (a) Number, (b) density potential temperature perturbation, and (c) equivalent radius of cold pools for different simulations as a function of time and/or synoptic forcing. The density potential temperature perturbation is averaged over each cold pool object and indicates the strength of the cold pools, with lower values (negative) for stronger, i.e., colder and denser, cold pools [Colour figure can be viewed at wileyonlinelibrary.com]

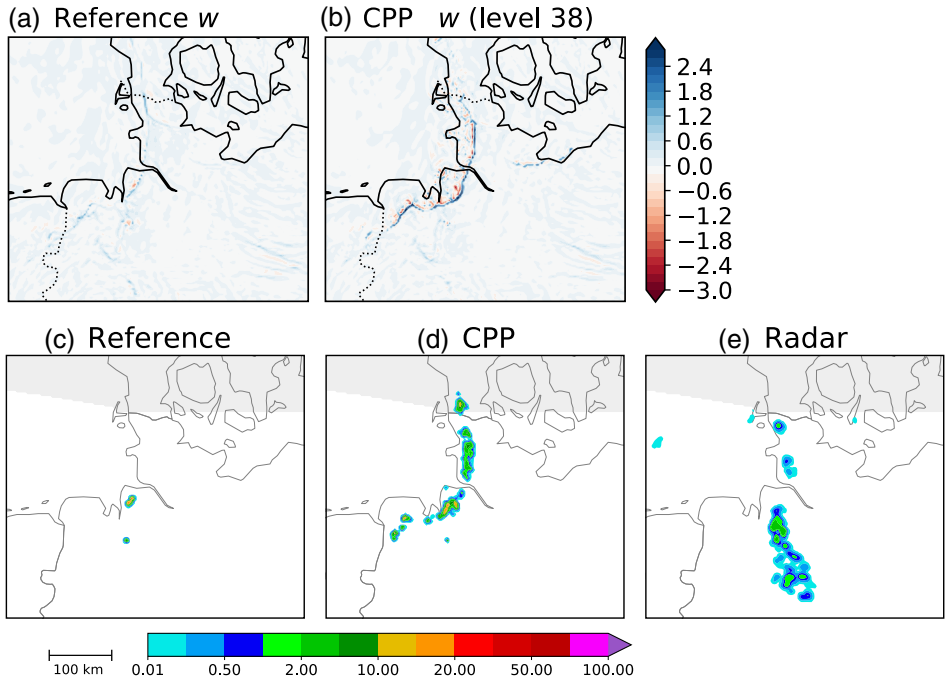

FIGURE 10 Illustrations for the sea breeze on 6 June 2016 at 1500 UTC for a small subdomain over the coastal areas. (a, b) show vertical velocity at ≈1 km (model level 38) for (a) the reference and (b) the CPP simulation. (c, d) show corresponding precipitation fields, and (e) radar observations [Colour figure can be viewed at wileyonlinelibrary.com]

in our simulations reveals that CPP effectively strengthens sea breeze fronts and fosters the initiation of convection. Figure 10 shows one such example, where the CPP simulation produces a more pronounced sea breeze front (a,b) which triggers earlier and more intense convection (c,d). The radar-derived precipitation (Figure 10e) shows more precipitation than the reference simulation near the coast. This suggests that the sea breeze indeed triggered convection on that day, that the strength of this sea breeze triggering is potentially under-represented in the reference simulation, and that the sea breeze in the CPP simulation is likely more realistic.

5 | PARAMETER SENSITIVITIES OF CPP

The CPP scheme requires the specification of several parameters, as presented in Section 3.7. The impact of these values has been extensively tested and the results are summarized here. There is a strong sensitivity to the scaling parameter α_{cp} which changes the target vertical velocity w_0 and hence directly influences the magnitude of the perturbations. Figures 7 and 8 show that a larger value of α_{cp} leads to increased precipitation amount, higher FSS and stronger impact on S-SAL. As Figure 1 shows, the amplitude of the perturbations also depends on the adjustment timescale τ_{cp}. Figures 7 and 8 show another simulation where both α_{cp} and τ_{cp} are changed, but with their ratio held constant (see simulation with $\alpha_{cp} = 0.3$, $\tau_{rmcp} = 300$). This simulation is very similar to the default CPP simulation, suggesting that changes in α_{cp} can be largely compensated by changes in τ_{cp}. Hence the CPP scheme behaves similarly to the early phase in Figure 1, where the ratio α_{cp}/τ_{cp} determines the magnitude of the perturbations, rather than α_{cp} alone. This interpretation is consistent with the finding from Figure 2, that the target vertical velocity is not fully reached.

A large number of sensitivity tests were carried out for the 5 June 2016 case, and the results for selected parameters and selected model output diagnostics, averaged over 1200–2000 UTC, are shown in Figure 11. In line with the previous findings, increased values of α_{cp} lead to increases in FSS, S-SAL, and slightly larger cloud sizes. For the most part, increases in τ_{cp} have the opposite effect.

The sensitivity to changing the vertical structure of the perturbations is illustrated in Figure 11 by varying the depth scale H_0 over a range of values from 1,000 to 2,500 m. In general, if perturbations extend higher up, their impact on precipitation amplitude is stronger, and comparable to increasing α_{cp}. Very large values of H_0 lead to a nonlinear increase in precipitation rates. This is not accompanied by strong increases in S-SAL and cloud radius, showing that the clouds are becoming locally too intense, which likely results from the perturbations extending too high and unrealistically amplifying the cloud updraughts. To evaluate modifications in the cold pool gust front mask $\mathcal{M}_{cp}$, we tested changes of the vertical velocity threshold w^*_{max} (0.3–0.7 m·s^{-1}), but differences in the simulations are small and ambiguous (Figure 11).

To summarize, the most important parameter sensitivities are those that influence the amplitude of the perturbations. This suggests that, as long as physically reasonable values for the other parameters are chosen, it is sufficient

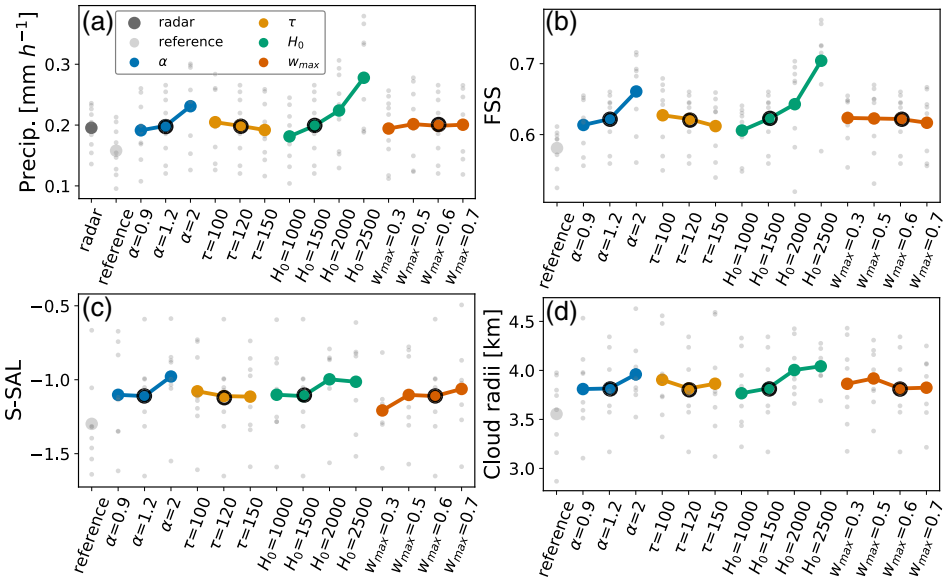

FIGURE 11 (a) Domain-averaged precipitation, (b) FSS, (c) S-SAL, and (d) cloud radii for for several different simulations on 5 June 2016 between 1200 and 2000 UTC. Large circles display average values in the time period, and the small grey points show values for each hour. The CPP simulations (all coloured) deviate from the default values only by one parameter as specified. The default CPP simulation is indicated by the black circle and included multiple times for better comparability. The cloud radii of radar observations have been omitted as they lie outside the displayed range. Figures 7 and 8 give the settings of the diagnostics [Colour figure can be viewed at wileyonlinelibrary.com]

to tune the single parameter α_{cp} to ensure a quantitatively realistic impact of CPP.

6 | SUMMARY AND CONCLUSIONS

In this work, we develop a Cold Pool Perturbation (CPP) scheme that adds increments to the vertical velocity in a convection-permitting model in order to strengthen cold pool gust fronts. Our hypothesis is that this will result in increased convective initiation, increased afternoon/evening precipitation and greater organization of convection. The perturbations are designed so that the vertical velocity in the lowest kilometre at cold pool gust fronts converges towards a target vertical velocity, which was obtained from dimensional analysis and estimated by local buoyancy gradients.

The cold pool perturbation scheme is implemented in the COSMO model of the German Weather Service, which has a horizontal resolution of about 2.8 km. Example fields of vertical velocity revealed stronger circulations at cold pool gust fronts with CPP compared to the reference simulation. Although the target vertical velocities are not fully reached, the hypothesized effect of the CPP scheme of strengthening the gust fronts is confirmed. Since cold pools are most prevalent during the day, the CPP scheme affects precipitation mainly at these times. On days with weak forcing of convection, and especially in the afternoon, total precipitation and the Fractions Skill Score (FSS) are improved. In addition, metrics for area-based convective organization, the S-SAL score and the average cell area indicate slightly stronger and more realistic organization during the weakly forced period. This coincides with our original expectations that cold-pool-driven convective initiation can strengthen existing precipitation cells and result in larger, more clustered/organized precipitation. However, the degree of organisation with CPP remains substantially less than in observations. On days with strong forcing, the effects of CPP are weaker and less beneficial, consistent with a lesser role of cold pools in triggering new convection. Similarly, Hirt *et al.* (2020) found a strong sensitivity of the relevance of cold-pool-driven convective initiation on the specific synoptic situation (e.g., on 29 May 2016, one of the strongly forced days, cold pools contributed only 20% of total convective initiation, while on 6 June 2016, one of the weakly forced days, cold pools contribute up to 50% in the afternoon). Overall, these results suggest a modest benefit of the CPP scheme in line with our original expectations, at least for the weakly forced period.

We also identified impacts of CPP on the cold pools themselves, with larger, more intense and more frequent cold pools in the CPP simulations, compared to the reference simulation. Results from Hirt *et al.* (2020) indicate that cold pools are generally too small and too weak in coarser resolution models, hence the more intense and larger cold pools in CPP may be an improvement in comparison to the real atmosphere. These findings further hint at a feedback loop by which stronger cold-pool-driven convective initiation by CPP strengthens the convection within the original cold pools and thereby the cold pool itself (Böing *et al.*, 2012; Schlemmer and Hohenegger,

2014; Hirt *et al.*, 2020). To better understand this feedback loop and the associated two-way interaction between precipitation and cold pools, a tracking of precipitation cells and cold pools throughout their lifetime may be necessary. Such an analysis would show whether the CPP scheme also extends the lifetimes of precipitation cells and cold pools, as the squall line formation theory of Rotunno *et al.* (1988) suggests.

An interesting side effect of CPP was to strengthen some sea breeze fronts. This effect could potentially be removed by adjusting the criteria for identifying gust fronts, but it may be preferable to include it. Since a sea breeze is also a form of a density current (e.g., Moncrieff and Liu, 1999), we would expect them to be weakened in low-resolution models, as for cold pools. Sea breeze fronts can also initiate new convection (e.g., Sun and Ogura, 1979; Johnson and Mapes, 2001), and hence it may be beneficial to apply the CPP scheme to them. Indeed, we identified an example where convective initiation by the sea breeze is improved.

As with any parametrization scheme, there are a number of parameter values that must be specified when the CPP scheme is deployed. An extensive set of sensitivity tests show that changing different parameters primarily leads to the same effect of changing the overall amount of convective initiation and hence precipitation. This is directly modified by the parameter α_{cp}, which scales the magnitude of the vertical velocity perturbations, so in practice it is probably sufficient to set the remaining parameters to physically reasonable values, and tune α_{cp} to give the best possible forecast performance.

Scale adaptivity is a crucial feature for grey zone parametrizations (Craig and Cohen, 2006; Berner *et al.*, 2017), and it is important to consider the applicability of the current CPP at different model resolutions. Certainly, CPP should only be applied if the models can explicitly resolve cold pools and deep convection. This likely limits CPP to resolutions below 10 km. The target vertical velocity is determined independently of the vertical velocity actually obtained at the model resolution, so the increments produced by the scheme will adapt to model error without explicit retuning. The same applies to other parameters such as depth scales that are based on physical properties of cold pools. Hence, in the limit of sufficiently small grid sizes to fully resolve cold pool gust fronts, w_{max} should converge to $\alpha_{\mathrm{cp}}\sqrt{BH}$, making the CPP scheme automatically ineffective (Equation (7)). However, the parameters used to define the mask where the perturbations are applied may need to be adjusted for different model resolutions. For example, the threshold value for orographic variability μ^*_{sso} used to suppress perturbations in mountain regions might need to change since μ^*_{sso} itself is resolution-dependent. Even more important is the threshold buoyancy gradient $\theta^*_{\mathrm{v,g}}$ used to identify cold pool boundaries. Since this is expressed as a buoyancy difference over a model grid length (Table 1), a basic dependence on resolution is included, but this will only be sufficient if the intensity of the cold pools, that is, the difference in buoyancy between cold pool and environment, is independent of resolution. This is not guaranteed (Hirt *et al.*, 2020; Squitieri and Gallus, 2020b), since the convective cloud dynamics, including downdraught strengths, are not well resolved in convection-permitting models.

Although the CPP scheme has improved most measures for the quality of the forecast convection, the improvements are modest and the differences to the observed properties of convection remain large. There are several other sources of model error which may account for some of these differences, but which also may interact with the CPP perturbations.

First, there are other sources of convective initiation that may replace or interact with cold pools. Examples of this include turbulent eddies in the convective boundary layer, and lifting over small-scale orographic features. These processes have been considered in previous work, and we have introduced the stochastic parametrizations, including PSP2, to improve their representation (Kober and Craig, 2016; Hirt *et al.*, 2019). These parametrizations gave useful increases in convective initiation, but tended to disrupt convective organisation. Since PSP2 and CPP are often active in different regions, it is difficult to anticipate how they would behave when applied together without extensive testing. Other land surface heterogeneities, such as soil moisture, also influence convective initiation, interact with cold pools and are insufficiently resolved in current models (Schlemmer and Hohenegger, 2014; Baur *et al.*, 2018; Grant and van den Heever, 2018; Keil *et al.*, 2019). In addition, the evolution of the convective clouds in a convection-permitting model may be poorly represented, producing errors in the precipitation, but also errors in cold pool properties which affect subsequent generations of clouds. This may result from poorly resolved updraughts and downdraughts, or inadequacies in other parametrizations such as cloud microphysics. An improved representation of cold pools can lead to better forecasts, but it is only a step along the way to improved forecasts of convective storms.

ACKNOWLEDGEMENTS

We thank C. Sackrenz for applying the cold pool detection which was required for producing Figure 9. The research leading to these results has been done within the subproject A6 of the Transregional Collaborative Research Center SFB/TRR 165 “Waves to Weather”

(www.wavestoweather.de) funded by the German Research Foundation (DFG).
Open access funding enabled and organized by Projekt DEAL.

ORCID

Mirjam Hirt https://orcid.org/0000-0002-5650-7594
George C. Craig https://orcid.org/0000-0002-7431-8164

REFERENCES

Bachmann, K., Keil, C., Weissmann, M. and Branch, A. (2019) Impact of radar data assimilation and orography on predictability of deep convection. *Quarterly Journal of the Royal Meteorological Society*, 145, 117–130. https://doi.org/10.1002/qj.3412.

Baldauf, M., Seifert, A., Förstner, J., Majewski, D., Raschendorfer, M. and Reinhardt, T. (2011) Operational convective-scale numerical weather prediction with the COSMO model: description and sensitivities. *Monthly Weather Review*, 139, 3887–3905. https://doi.org/10.1175/MWR-D-10-05013.1.

Baur, F., Keil, C. and Craig, G.C. (2018) Soil moisture–precipitation coupling over Central Europe: interactions between surface anomalies at different scales and the dynamical implication. *Quarterly Journal of the Royal Meteorological Society*, 144, 2863–2875.

Benjamin, T.B. (1968) Gravity currents and related phenomena. *Journal of Fluid Mechanics*, 31, 209–248. https://doi.org/10.1017/S0022112068000133.

Berner, J., Achatz, U., Batté, L., Bengtsson, L., de la Cámara, A., Christensen, H.M., Colangeli, M., Coleman, D.R.B., Crommelin, D., Dolaptchiev, S.I., Franzke, C.L.E., Friederichs, P., Imkeller, P., Järvinen, H., Juricke, S., Kitsios, V., Lott, F., Lucarini, V., Mahajan, S., Palmer, T.N., Penland, C., Sakradzija, M., von Storch, J.-S., Weisheimer, A., Weniger, M., Williams, P.D. and Yano, J.-I. (2017) Stochastic parameterization: toward a new view of weather and climate models. *Bulletin of the American Meteorological Society*, 98, 565–588. https://doi.org/10.1175/BAMS-D-15-00268.1.

Böing, S.J., Jonker, H.J.J., Siebesma, A.P. and Grabowski, W.W. (2012) Influence of the subcloud layer on the development of a deep convective ensemble. *Journal of the Atmospheric Sciences*, 69, 2682–2698.

Bryan, G.H. and Rotunno, R. (2008) Gravity currents in a deep anelastic atmosphere. *Journal of the Atmospheric Sciences*, 65, 536–556. https://doi.org/10.1175/2007JAS2443.1.

Bryan, G.H. and Rotunno, R. (2014) The optimal state for gravity currents in shear. *Journal of the Atmospheric Sciences*, 71, 448–468. https://doi.org/10.1175/JAS-D-13-0156.1.

Cafaro, C. and Rooney, G.G. (2018) Characteristics of colliding density currents: a numerical and theoretical study. *Quarterly Journal of the Royal Meteorological Society*, 144, 1761–1771.

Chagnon, J.M. and Bannon, P.R. (2005) Adjustment to injections of mass, momentum, and heat in a compressible atmosphere. *Journal of the Atmospheric Sciences*, 62, 2749–2769. https://doi.org/10.1175/JAS3503.1.

Clark, P.A., Roberts, N.M., Lean, H.W., Ballard, S.P. and Charlton-Perez, C. (2016) Convection-permitting models: a step-change in rainfall forecasting. *Meteorological Applications*, 23, 165–181. https://doi.org/10.1002/met.1538.

Craig, G.C. and Cohen, B.G. (2006) Fluctuations in an equilibrium convective ensemble. Part I: theoretical formulation. *Journal of the Atmospheric Sciences*, 63, 1996–2004. https://doi.org/10.1175/JAS3709.1.

Deutscher Wetterdienst (2018a). Hoch aufgelöste Niederschlgsanalyse und -vorhersage auf der Basis quantitativer Radar- und Omrometerdaten für grenzüberschreitende Fluss-Einzugsgebiete von Deutschland im Echtzeitbetrieb – Beschreibung des Kompositsformats Version 2.4.4. Available at: https://www.dwd.de/DE/leistungen/radolan/radolan_info/radolan_radvor_op_komposit_format_pdf.pdf; accessed 3 April 2021.

Deutscher Wetterdienst (2018b). RADOLAN/RADVOR Produktübersicht. Available at: https://www.dwd.de/DE/leistungen/radolan/produktuebersicht/radolan_produktuebersicht_pdf.pdf; accessed 3 April 2021.

Doms, G., Förstner, J., Heise, E., Herzog, H.J., Mironov, D., Raschendorfer, M., Reinhardt, T., Ritter, B., Schrodin, R., Schulz, J.-P. and Vogel, G. (2011) *A Description of the Nonhydrostatic Regional COSMO Model. Part II: Physical Parameterization*. Offenbach: Deutscher Wetterdienst.

Done, J.M., Craig, G.C., Gray, S.L., Clark, P.A. and Gray, M.E.B. (2006) Mesoscale simulations of organized convection: importance of convective equilibrium. *Quarterly Journal of the Royal Meteorological Society*, 132, 737–756. https://doi.org/10.1256/qj.04.84.

Dueben, P.D., Wedi, N., Saarinen, S. and Zeman, C. (2020) Global simulations of the atmosphere at 1.45 km grid-spacing with the integrated forecasting system. *Journal of the Meteorological Society of Japan. Series II*, 98, 551–572.

ECMWF (2016). The strength of a common goal – a roadmap to 2025. Available at: https://www.ecmwf.int/sites/default/files/ECMWF_Roadmap_to_2025.pdf; accessed 7 November 2019.

Edson, A.R. and Bannon, P.R. (2008) Nonlinear atmospheric adjustment to thermal forcing. *Journal of the Atmospheric Sciences*, 62, 4253–4272.

Feng, Z., Hagos, S., Rowe, A.K., Burleyson, C.D., Martini, M.N. and de Szoeke, S.P. (2015) Mechanisms of convective cloud organization by cold pools over tropical warm ocean during the AMIE/-DYNAMO field campaign. *Journal of Advances in Modeling Earth Systems*, 7, 357–381. https://doi.org/10.1002/2014MS000384.

Fiedler, B.H. (2002) A wind transform for acoustic adjustment in compressible models. *Monthly Weather Review*, 130, 741–746. https://doi.org/10.1175/1520-0493(2002)130<0741:AWTFAA>2.0.CO;2.

Flack, D.L., Gray, S.L., Plant, R.S., Lean, H.W. and Craig, G.C. (2018) Convective-scale perturbation growth across the spectrum of convective regimes. *Monthly Weather Review*, 146, 387–405.

Grandpeix, J.Y. and Lafore, J.P. (2010) A density current parameterization coupled with Emanuel's convection scheme. Part I: the models. *Journal of the Atmospheric Sciences*, 67, 881–897. https://doi.org/10.1175/2009JAS3044.1.

Grandpeix, J.Y., Lafore, J.P. and Cheruy, F. (2010) A density current parameterization coupled with Emanuel's convection scheme. Part II: 1D simulations. *Journal of the Atmospheric Sciences*, 67, 898–922. https://doi.org/10.1175/2009JAS3045.1.

Grant, L.D. and van den Heever, S.C. (2016) Cold pool dissipation. *Journal of Geophysical Research: Atmospheres*, 121, 1138–1155.

Grant, L.D. and van den Heever, S.C. (2018) Cold pool–land surface interactions in a dry continental environment. *Journal of Advances in Modeling Earth Systems*, 10, 1513–1526. https://doi.org/10.1029/2018MS001323.

Haerter, J.O., Boeing, S.J., Henneberg, O. and Nissen, S.B. (2018) Reconciling cold pool dynamics with convective self-organization. *arXiv Preprint*. arXiv:1810.05518

Hanley, K.E., Plant, R.S., Stein, T.H.M., Hogan, R.J., Nicol, J.C., Lean, H.W., Halliwell, C. and Clark, P.A. (2015) Mixing-length controls on high-resolution simulations of convective storms. *Quarterly Journal of the Royal Meteorological Society*, 141, 272–284.

Hirt, M., Craig, G.C., Schäfer, S.A.K., Savre, J. and Heinze, R. (2020) Cold-pool-driven convective initiation: using causal graph analysis to determine what convection-permitting models are missing. *Quarterly Journal of the Royal Meteorological Society*, 146, 2205–2227. https://doi.org/10.1002/qj.3788.

Hirt, M., Rasp, S., Blahak, U. and Craig, G.C. (2019) Stochastic parameterization of processes leading to convective initiation in kilometer-scale models. *Monthly Weather Review*, 147, 3917–3934. https://doi.org/10.1175/MWR-D-19-0060.1.

Hoyer, S. and Hamman, J. (2017) xarray: N-D labeled arrays and datasets in Python. *Journal of Open Research Software*, 5. https://doi.org/10.5334/jors.148.

Hunter, J.D. (2007) Matplotlib: a 2D graphics environment. *Computing in Science & Engineering*, 9, 90–95. https://doi.org/10.1109/MCSE.2007.55.

Jeevanjee, N. (2017) Vertical velocity in the gray zone. *Journal of Advances in Modeling Earth Systems*, 9, 2304–2316. https://doi.org/10.1002/2017MS001059.

Jeevanjee, N. and Romps, D.M. (2016) Effective buoyancy at the surface and aloft. *Quarterly Journal of the Royal Meteorological Society*, 142, 811–820. https://doi.org/10.1002/qj.2683.

Johnson, R.H. and Mapes, B.E. (2001). Mesoscale Processes and Severe Convective Weather, pp. 71–122 in Severe Convective Storms, Meteorological Monographs. Boston, MA: American Meteorological Society, DOI 10.1007/978-1-935704-06-5_3, (to appear in print).

Judt, F. (2018) Insights into atmospheric predictability through global convection-permitting model simulations. *Journal of the Atmospheric Sciences*, 75, 1477–1497. https://doi.org/10.1175/JAS-D-17-0343.1.

Keil, C., Baur, F., Bachmann, K., Rasp, S., Schneider, L. and Barthlott, C. (2019) Relative contribution of soil moisture, boundary-layer and microphysical perturbations on convective predictability in different weather regimes. *Quarterly Journal of the Royal Meteorological Society*, 145, 3102–3115. https://doi.org/10.1002/qj.3607.

Kober, K. and Craig, G.C. (2016) Physically Based Stochastic Perturbations (PSP) in the boundary layer to represent uncertainty in convective initiation. *Journal of the Atmospheric Sciences*, 73, 2893–2911. https://doi.org/10.1175/JAS-D-15-0144.1.

Leoncini, G., Plant, R.S., Gray, S.L. and Clark, P.A. (2010) Perturbation growth at the convective scale for CSIP IOP18. *Quarterly Journal of the Royal Meteorological Society*, 136, 653–670.

Leutwyler, D., Lüthi, D., Ban, N., Fuhrer, O. and Schär, C. (2017) Evaluation of the convection-resolving climate modeling approach on continental scales. *Journal of Geophysical Research: Atmospheres*, 122, 5237–5258. https://doi.org/10.1002/2016JD026013.

Markowski, P. and Richardson, Y. (2011) *Mesoscale Meteorology in Midlatitudes*. Chichester: John Wiley & Sons.

McKinney, W. (2010). Data structures for statistical computing in Python. In S. van der Walt and J. Millman (Eds.), *Proceedings of the 9th Python in Science Conference*, Vol. 445, pp. 51–56. https://doi.org/10.25080/Majora-92bf1922-00a.

Meyer, B. and Haerter, J.O. (2020) Mechanical forcing of convection by cold pools: collisions and energy scaling. *Journal of Advances in Modeling Earth Systems*, 12(11). https://doi.org/10.1029/2020MS002281.

Moncrieff, M.W. and Liu, C. (1999) Convection initiation by density currents: role of convergence, shear, and dynamical organization. *Monthly Weather Review*, 127, 2455–2464. https://doi.org/10.1175/1520-0493(1999)127<2455:CIBDCR>2.0.CO;2.

Morrison, H. (2016a) Impacts of updraft size and dimensionality on the perturbation pressure and vertical velocity in cumulus convection. Part I: simple, generalized analytic solutions. *Journal of the Atmospheric Sciences*, 73, 1441–1454.

Morrison, H. (2016b) Impacts of updraft size and dimensionality on the perturbation pressure and vertical velocity in cumulus convection. Part II: comparison of theoretical and numerical solutions and fully dynamical simulations. *Journal of the Atmospheric Sciences*, 73, 1455–1480.

Moseley, C., Pscheidt, I., Cioni, G. and Heinze, R. (2020) Impact of resolution on large-eddy simulation of midlatitude summertime convection. *Atmospheric Chemistry and Physics*, 20, 2891–2910. https://doi.org/10.5194/acp-20-2891-2020.

Palmer, T.N. (2019) The ECMWF ensemble prediction system: looking back (more than) 25 years and projecting forward 25 years. *Quarterly Journal of the Royal Meteorological Society*, 145, 12–24. https://doi.org/10.1002/qj.3383.

Panosetti, D., Schlemmer, L. and Schär, C. (2019) Bulk and structural convergence at convection-resolving scales in real-case simulations of summertime moist convection over land. *Quarterly Journal of the Royal Meteorological Society*, 145, 1427–1443. https://doi.org/10.1002/qj.3502.

Park, S. (2014) A Unified Convection Scheme (UNICON). Part I: formulation. *Journal of the Atmospheric Sciences*, 71, 3902–3930. https://doi.org/10.1175/JAS-D-13-0233.1.

Pauluis, O. and Garner, S. (2006) Sensitivity of radiative-convective equilibrium simulations to horizontal resolution. *Journal of the Atmospheric Sciences*, 63, 1910–1923. https://doi.org/10.1175/JAS3705.1.

Piper, D., Kunz, M., Ehmele, F., Mohr, S., Mühr, B., Kron, A. and Daniell, J. (2016) Exceptional sequence of severe thunderstorms and related flash floods in May and June 2016 in Germany – Part 1: meteorological background. *Natural Hazards and Earth System Sciences*, 16, 2835–2850. https://doi.org/10.5194/nhess-16-2835-2016.

Rasp, S., Selz, T. and Craig, G.C. (2018) Variability and clustering of midlatitude summertime convection: testing the Craig and Cohen theory in a convection-permitting ensemble with stochastic boundary-layer perturbations. *Journal of the Atmospheric Sciences*, 75, 691–706. https://doi.org/10.1175/JAS-D-17-0258.1.

Reif, D.W., Bluestein, H.B., Weckwerth, T.M., Wienhoff, Z.B. and Chasteen, M.B. (2020) Estimating the maximum vertical velocity at the leading edge of a density current. *Journal of the Atmospheric Sciences*, 77, 3683–3700. https://doi.org/10.1175/JAS-D-20-0028.1.

Roberts, N.M. and Lean, H.W. (2008) Scale-selective verification of rainfall accumulations from high-resolution forecasts of convective events. *Monthly Weather Review*, 136, 78–97. https://doi.org/10.1175/2007MWR2123.1.

Rotunno, R., Klemp, J.B. and Weisman, M.L. (1988) A theory for strong, long-lived squall lines. *Journal of the Atmospheric Sciences*, 45, 463–485.

Rozbicki, J.J., Young, G.S. and Qian, L. (1999) Test of a convective wake parameterization in the single-column version of CCM3. *Monthly Weather Review*, 127, 1347–1361. https://doi.org/10.1175/1520-0493(1999)127<1347:TOACWP>2.0.CO;2.

Schär, C., Fuhrer, O., Arteaga, A., Ban, N., Charpilloz, C., Di Girolamo, S., Hentgen, L., Hoefler, T., Lapillonne, X., Leutwyler, D., Osterried, K., Panosetti, D., Rüdisühli, S., Schlemmer, L., Schulthess, T., Sprenger, M., Ubbiali, S. and Wernli, H. (2019) Kilometer-scale climate models: prospects and challenges. *Bulletin of the American Meteorological Society*, 101, E567–E587. https://doi.org/10.1175/BAMS-D-18-0167.1.

Schättler, U., Doms, G. and Schraff, C. (2016) *A Description of the Non-hydrostatic Regional COSMO Model, Part VII: User's Guide*. Offenbach: Consortium for Small-Scale Modelling (COSMO), Deutscher Wetterdienst.

Schlemmer, L. and Hohenegger, C. (2014) The formation of wider and deeper clouds as a result of cold-pool dynamics. *Journal of the Atmospheric Sciences*, 71, 2842–2858.

Schraff, C., Reich, H., Rhodin, A., Schomburg, A., Stephan, K., Periáñez, A. and Potthast, R. (2016) Kilometre-scale ensemble data assimilation for the COSMO model (KENDA). *Quarterly Journal of the Royal Meteorological Society*, 142, 1453–1472. https://doi.org/10.1002/qj.2748.

Senf, F., Klocke, D. and Brueck, M. (2018) Size-resolved evaluation of simulated deep tropical convection. *Monthly Weather review*, 146, 2161–2182.

Squitieri, B.J. and Gallus, W.A. (2020) On the forecast sensitivity of MCS cold pools and related features to horizontal grid spacing in convection-allowing WRF simulations. *Weather and Forecasting*, 35, 325–346. https://doi.org/10.1175/WAF-D-19-0016.1.

Stein, T.H.M., Scovell, R.W., Hanley, K.E., Lean, H.W. and Marsden, N.H. (2020) The potential use of operational radar network data to evaluate the representation of convective storms in NWP models. *Quarterly Journal of the Royal Meteorological Society*, 146, 2315–2331. https://doi.org/10.1002/qj.3793.

Stevens, B., Satoh, M., Auger, L., Biercamp, J., Bretherton, C., Düben, P., Judt, F., Khairoutdinov, M., Klocke, D., Kornblueh, L., Kodama, C., Neumann, P., Lin, S., Putman, W.M., Röber, N., Shibuya, R., Vidale, P. and Wedi, N. (2019) DYAMOND: the dynamics of the atmospheric general circulation modeled on non-hydrostatic domains. *Progress in Earth and Planetary Science*, 6. https://doi.org/10.1186/s40645-019-0304-z.

Sun, W.-Y. and Ogura, Y. (1979) Boundary-layer forcing as a possible trigger to a squall-line formation. *Journal of the Atmospheric Sciences*, 36, 235–254. https://doi.org/10.1175/1520-0469(1979)036<0235:BLFAAP>2.0.CO;2.

Tompkins, A.M. (2001) Organization of tropical convection in low vertical wind shears: the role of water vapor. *Journal of the Atmospheric Sciences*, 58, 529–545.

Torri, G. and Kuang, Z. (2019) On cold pool collisions in tropical boundary layers. *Geophysical Research Letters*, 46, 399–407.

van der Walt, S., Colbert, S.C. and Varoquaux, G. (2011) The NumPy array: a structure for efficient numerical computation. *Computing in Science Engineering*, 13, 22–30. https://doi.org/10.1109/MCSE.2011.37.

Virtanen, P., Gommers, R., Oliphant, T.E., Haberland, M., Reddy, T., Cournapeau, D., Burovski, E., Peterson, P., Weckesser, W., Bright, J., van der Walt, S.J., Brett, M., Wilson, J., Jarrod Millman, K., Mayorov, N., Nelson, A.R.J., Jones, E., Kern, R., Larson, E., Carey, C., Polat, İ., Feng, Y., Moore, E.W., van der Plas, J., Laxalde, D., Perktold, J., Cimrman, R., Henriksen, I., Quintero, E.A., Harris, C.R., Archibald, A.M., Ribeiro, A.H., Pedregosa, F. and van Mulbregt, P. (2019) SciPy 1.0 – fundamental algorithms for scientific computing in Python. *arXiv e-prints*. arXiv:1907.10121

von Kármán, T. (1940) The engineer grapples with nonlinear problems. *Bulletin of the American Mathematical Society*, 46, 615–684. https://doi.org/10.1090/S0002-9904-1940-07266-0.

Waskom, M. (2021) Seaborn: statistical data visualization. *Journal of Open Source Software*, 6(60), 3021. http://dx.doi.org/10.21105/joss.03021.

Weisman, M.L. and Rotunno, R. (2004) "A theory for strong long-lived squall lines" revisited. *Journal of the Atmospheric Sciences*, 61, 361–382. https://doi.org/10.1175/1520-0469(2004)061<0361:ATFSLS>2.0.CO;2.

Weisman, M.L., Skamarock, W.C. and Klemp, J.B. (1997) The resolution dependence of explicitly modeled convective systems. *Monthly Weather Review*, 125, 527–548.

Wernli, H., Paulat, M., Hagen, M. and Frei, C. (2008) SAL-A novel quality measure for the verification of quantitative precipitation forecasts. *Monthly Weather Review*, 136, 4470–4487.

Wernli, H., Hofmann, C. and Zimmer, M. (2009) Spatial forecast verification methods intercomparison project: application of the SAL technique. *Weather and Forecasting*, 24, 1472–1484. https://doi.org/10.1175/2009WAF2222271.1.

Zhou, L., Lin, S.-J., Chen, J.-H., Harris, L.M., Chen, X. and Rees, S.L. (2019) Toward convective-scale prediction within the next generation global prediction system. *Bulletin of the American Meteorological Society*, 100, 1225–1243.

How to cite this article: Hirt M, Craig GC. A cold pool perturbation scheme to improve convective initiation in convection-permitting models. *Q.J.R. Meteorol. Soc.* 2021;147:2429–2447. https://doi.org/10.1002/qj.4032

APPENDIX A. DIMENSIONAL ANALYSIS OF GUST FRONT VERTICAL VELOCITIES

Here, we give the full derivation for a characteristic vertical velocity scale W for cold pool gust fronts, which is used in Section 3.1. We consider the inviscid, Boussinesque approximated set of equations for the streamfunction Φ, vorticity η and vertical velocity w in a two-dimensional plane in x and z, which is often considered for density

currents (Rotunno *et al.*, 1988; Weisman and Rotunno, 2004; Bryan and Rotunno, 2014):

$$\begin{aligned}\frac{\mathrm{d}\eta}{\mathrm{d}t} &= -\frac{\partial b}{\partial x},\\ \nabla^2\Phi &= \eta,\\ w &= -\frac{\partial \Phi}{\partial x},\\ \text{and } w &= \frac{\mathrm{d}z}{\mathrm{d}t}.\end{aligned}$$

We consider a parcel situated at a horizontal, time-independent buoyancy gradient $\partial b/\partial x$ (i.e., a cold pool gust front). First, we non-dimensionalize the equations using characteristic scales B, H, L, W, η^*, Φ^* and non-dimensional variables denoted by a tilde, for example, $\widetilde{x}$:

$$b = B\widetilde{b}, \quad x = L\widetilde{x}, \quad z = H\widetilde{x},$$
$$t = T\widetilde{t}, \quad w = W\widetilde{w}, \quad \eta = \eta^*\widetilde{\eta}, \quad \Phi = \Phi^*\widetilde{\Phi}.$$

The non-dimensional variables here represent functions that depend only on other non-dimensional variables. This gives the following transformed set of equations:

$$\begin{aligned}\frac{\mathrm{d}\widetilde{\eta}}{\mathrm{d}\widetilde{t}} &= -\frac{BT}{\eta^* L}\frac{\partial \widetilde{b}}{\partial \widetilde{x}},\\ \frac{\partial \widetilde{\Phi}}{\partial \widetilde{x}^2} &= \frac{\eta^*}{\Phi^*\left(\frac{1}{L^2}+\frac{1}{H^2}\right)}\widetilde{\eta},\\ \widetilde{w} &= -\frac{\Phi^*}{WL}\frac{\partial \widetilde{\Phi}}{\partial \widetilde{x}},\\ \text{and } \widetilde{w} &= \frac{H}{WT}\frac{\mathrm{d}\widetilde{z}}{\mathrm{d}\widetilde{t}}.\end{aligned}$$

The dimensionless factors consisting only of characteristic scales on the right-hand side can be set to equal to 1, by determining values for η^*, ϕ^*, T and W accordingly:

$$\begin{aligned}\eta^* &= \frac{BT}{L},\\ \Phi^* &= \frac{\eta^*}{\left(\frac{1}{L^2}+\frac{1}{H^2}\right)},\\ W &= \frac{\Phi^*}{L},\\ T &= \frac{H}{W}.\end{aligned}$$

Substituting the first, second and last equation into the third, we obtain the following relationship for W:

$$W = \sqrt{\frac{BH}{1+\frac{L^2}{H^2}}},$$

which describes the characteristic vertical velocity scale within a circulation driven by horizontal buoyancy gradients and how it depends on both the horizontal and vertical length-scales L and H in addition to the characteristic buoyancy scale B.

Since the preceding expression comes from a general dimensional analysis for circluations driven by a buoyancy anomaly, it is not surprising that similar relationships can be obtained for other geometries. In particular, the ascent rates for rising warm bubbles with different aspect ratios has been investigated by Weisman *et al.* (1997), Pauluis and Garner (2006), Morrison (2016a), Morrison (2016b), Jeevanjee and Romps (2016) and Jeevanjee (2017). They found that the deceleration of a buoyant air parcel caused by the need to displace the air around it depends on the horizontal extent L and the vertical extent H of the buoyancy acceleration: for thin and tall parcels ($L/H \approx 1$), the deceleration is moderate while for wide and flat parcels ($L/H \gg 1$) the deceleration is larger as substantially more air has to be displaced. As a result, the characteristic vertical velocities have a dependence on L/H similar to Equation (1).

APPENDIX B. COMPUTATIONAL ASPECTS

The source code for COSMO, the run scripts and the simulation data can be made available upon request. The analysis of the simulation output was mostly done using open source tools within a Python framework and with Jupyter notebooks. The code and the notebooks are available on https://github.com/HirtM/The_CPP_Scheme (accessed 3 April 2021). The notebooks further include more background information and examples. Mostly, the following packages were used: numpy (van der Walt *et al.*, 2011), scipy (Virtanen *et al.*, 2019), xarray (Hoyer and Hamman, 2017), pandas (McKinney, 2010), seaborn (Waskom *et al.*, 2021), matplotlib (Hunter, 2007) and enstools. The Python package enstools is currently under development within the 'Waves to Weather' project (www.wavestoweather.de) and is designed for processing atmospheric ensemble simulations. It can be made available upon request.

APPENDIX C. THE STRUCTURE COMPONENT OF THE SAL SCORE

A quantitative object-based measure for the structure of the precipitation field is the S(tructure) component of the SAL score (Wernli *et al.*, 2008). It is based on comparing the normalized area and intensity of precipitation objects between observations (radar) and model output. Precipitation objects are identified using the threshold R^* as suggested by Wernli *et al.* (2009), where $R^* = 1/15 R_{95}$ and R_{95} corresponds to the 95th percentile of precipitation at grid points exceeding 0.1 mm·hr^{-1}. We compute R_{95} separately for radar and forecast and for each time step. Negative S values imply that the simulated precipitation cells are too small and peaked compared to the radar observations, while $S = 0$ suggests a perfect match in terms of structure.

APPENDIX D. COLD POOL DETECTION

The cold pool detection scheme from Hirt *et al.* (2020) is used to detect cold pool objects and has been adapted to the different model set-up used here.

To detect cold pools, the density potential temperature

$$\theta_\rho = \theta(1 + 0.608 r_\mathrm{v} - r_\mathrm{w} - r_\mathrm{i} - r_\mathrm{r} - r_\mathrm{s} - r_\mathrm{g})$$

(averaged approximately over the lowest 200 m) and precipitation are used (model level 45–50). Here θ denotes the potential temperature, r_v the water vapour mixing ratio and r_w, r_i, r_r, r_s and r_g the mixing ratios of liquid cloud water, cloud ice, rain, snow and graupel respectively. A local perturbation in density potential temperature, $\theta'_{\rho,0}$, is calculated by subtracting a moving average, $\overline{\theta_\rho}^m$, of filter size 30 pixels (≈84 km) horizontally and 2 hr in time with reflection at the boundaries. The perturbations are further calibrated by subtracting the domain-mean density potential temperature perturbation: $\theta'_\rho = \theta'_{\rho,0} - \overline{\theta'_{\rho,0}}$. Then preliminary cold pools are identified as regions with $\theta'_\rho < -1.2$K and separated by the watershed-merge segmentation method of Senf *et al.* (2018). We exclude cold pool objects smaller than 24 pixels, that is, with an equivalent diameter of ≈15 km, roughly corresponding to the effective model resolution ($5\Delta x$). We also exclude cold areas that are not caused by convective downdraughts by using an additional precipitation criterion: at least one grid box of the cold pool object must have precipitation >4 mm·hr^{-1}. In addition, we remove cold pools over the sea and over the Alps, since objects are otherwise identified there, which are likely not associated to cold pools (see Jupyter notebooks on https://github.com/HirtM/The_CPP_Scheme for the specific extent of the mask).

Further details can be found in Hirt *et al.* (2020) or the Jupyter notebooks. The main differences of the cold pool detection here from Hirt *et al.* (2020) concern the used thresholds. Due to different grid sizes used here, the criteria for minimum cold pool size is different. Also the precipitation threshold and the density potential temperature perturbation threshold have been adapted to detect most cold pools in our simulations. Since a larger model domain is used, which includes the Alps, the rectangular box over the Alps was newly introduced for our simulations. We have tested also other thresholds and used those which seemed to give the best cold pool detection for our simulations. Example fields of detected cold pools can be found in the Jupyter notebooks.